

pubs.acs.org/cm Article

Porous Semiconducting K-Sn-Mo-S Aerogel: Synthesis, Local Structure, and Ion-Exchange Properties

Alicia Blanton, Taohedul Islam, Subrata Chandra Roy, Ahmet Celik, Jing Nie, David R. Baker, Dien Li, Kathryn Taylor-Pashow, Xianchun Zhu, Avijit Pramanik, Ruhul Amin, Renfei Feng, Roman Chernikov, and Saiful M. Islam*



Cite This: https://doi.org/10.1021/acs.chemmater.3c01675



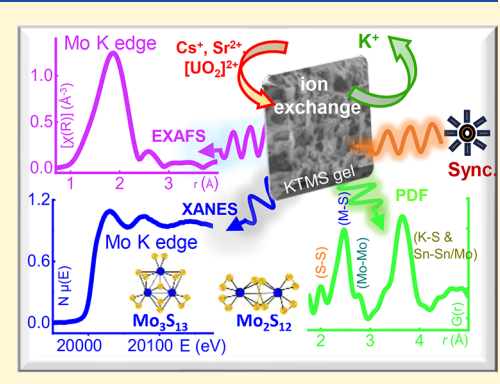
ACCESS

Metrics & More

Article Recommendations

s Supporting Information

ABSTRACT: Chalcogenide-based aerogels are emerging porous semiconducting nanomaterials that appeal to applications in clean energy and the environment. Here, we report a novel gel, potassium—tin—molybdenum—sulfides (KTMS), that integrates the electrostatically bound K^+ ions in the covalent network of Sn—Mo—S. Its gelation requires a concurrent reduction of $Mo^{6+} \rightarrow Mo^{4+/5+}$ and the oxidation of $S^{2-} \rightarrow S^{n^-}$ ($n \approx 1$) and $Sn^{2+} \rightarrow Sn^{4+}$. KTMS is an amorphous semiconductor showing quantum confinement effects on band gap energies, $2.1 \rightarrow 1.4 \rightarrow 0.9$ eV for its wet- \rightarrow aero- \rightarrow xerogels. Synchrotron X-ray pair distribution function (PDF) and extended X-ray absorption fine structure (EXAFS) revealed a complex local structure of KTMS consisting of molecular $Mo_2(S_2)_6$ and $Mo_3S(S_2)_6$ clusters. In addition, the Sn–S coordination is related to crystalline $Na_4Sn_3S_8$ and SnS_2 . KTMS also demonstrated the removal of the radionuclides of Cs^+ , Sr^{2+} , and UO_2^{2+} from ppm to ppb levels with distribution constants (K_d) up to $\geq 10^4$ mL/g.



Notably, despite the lack of atomic periodicity in the amorphous KTMS, the K^+ ion is ion-exchangeable with chemically diverse Sr^{2+} , Cs^+ , and UO_2^{2+} in aqueous solutions; especially the ion-exchange properties of Sr^{2+} and $UO_2^{2+} \equiv (O = U = O)^{2+}$ is not known to any chalcogels known to date. The sequestration of Cs^+ and Sr^{2+} was achieved by the exchange of K^+ in the amorphous KTMS, and the removal of $[O = U^{6+} = O]^{2+}$ synergistically involves surface sorption via $-S\cdots U^{6+} = O_2^{2+}$ covalent interactions and ion-exchange via the hard-soft Lewis acid-base paradigm. Overall, cooperative roles played by the diverse bonding motifs, surface-exposed Lewis basic frameworks, and polarizability of the (poly)sulfides make it an exceptional adsorbent for chemically diverse radioactive species. This finding will guide the design of superior sorbents for chemically distinct metal ion separation.

■ INTRODUCTION

Chalcogenide-based aerogels are an emerging class of porous panoscopic materials that consist of (poly)chalcogenide and/ or metal chalcogenide anionic clusters. $^{1-6}$ This class of materials possesses remarkable interest because of their unique properties, such as surface polarizability, Lewis basicity, semiconductivity, and random porosities among the interconnected nanoparticles. Integration of these features enables chalcogels to find applications in sustainable energy and environmental technologies that include, but are not limited to, electro- and photocatalysis, $^{7-10}$ electrochemical energy storage, 11 hydrodesulfurization catalysis, 12 and environmental remediation of hazardous aqueous and gaseous pollutants. $^{13-18}$

The chalcogenide-based aerogel was first discovered in the early-2000s by Brock and co-workers for binary metal chalcogenides and proposed a general synthetic strategy that entails oxidative aggregation of metal chalcogenide nanoparticle building blocks. Later, Kanatzidis and co-workers reported another synthetic strategy using metal chalcogenide clusters which allowed the expansion of their chemistry with diverse chemical compositions and named the materials

"chalcogels".⁴ To date, the synthesis of chalcogenide-based gels was accomplished in different synthetic routes, namely thiolysis, nanoparticle condensation, oxidative coupling, and metathesis. ^{5,6,14,20} The metathesis synthesis route utilizes the salts of chalcogenide clusters and metal linkers where the anionic building blocks of the chalcogenide clusters are crosslinked by metal cations to form molecular size entities which then extend in a polymer-like network. Since the discovery of chalcogels, a large variety of chalcogenide clusters, such as $[MQ_4]^{4-}$, $[M_2Q_6]^{4-}$, and $[M_4Q_{10}]^{4-}$ (M = Ge, Sn; Q = S, Se), $[MQ_4]^{2-}$ and $[M_3Q_{13}]^{2-}$ (M = Mo; Q = S, Se), $[MQ_3]^{3-}$ (M = Sb, As; Q = S), $[MTe_3]^{3-}$ (M = Sb, Bi) and polysulfide ligands S_x^{2-} (x = 4,5,6), have been identified to form chalcogels in

Received: July 4, 2023 Revised: November 6, 2023 Accepted: November 7, 2023



conjunction with transition and p-block metal linkers. 7,12,14,17,21-32 The formation of the chalcogel is mainly attributed to covalent interactions of soft polarizable sulfide and transition metal or p-block cations. The presence of alkali metal cations can introduce electrostatic interactions in the covalent network of chalcogels, which can be exchanged with cations with a greater affinity toward chemically soft Lewis basic (poly)sulfide network of the chalcogel in accordance with Pearson's hard and soft Lewis acid-base paradigm (HSAB).³³ The ion exchange properties of the chalcogel were reported for amorphous KPtS_{w}^{32} (NH₄)_{0.03}MoS_w¹⁴ and nanocrystalline $\text{KCo}_{6}\text{S}_{21}$, ³⁴ where K⁺ and NH₄⁺ ions were exchanged with Cs⁺, and/or K⁺. In addition, crystalline layered metal sulfides, such as $K_{2x}Mn_xSn_{3-x}S_6$ (x = 0.5-0.95, KMS-1)³⁵ and $K_{2x}Sn_{4-x}S_{8-x}$ (x = 0.65-1, KTS-3), (x = 0.65-1, KTS-3) are attributed to the separation of UO22+, Cs+, Sr2+ and heavy metals cations37 from aqueous solution by integrating these ions into their interlayered space by ion exchange. Notably, the linear geometry of the UO₂²⁺ $(O=U=O)^{2+}$ ion facilitates its intercalation by the exchange of the K⁺ ion of KMS-1 and KTS-3.³⁶ Hence, by integrating the ion exchange properties of amorphous chalcogels and crystalline layered metal sulfides, one may presume that the alkali metal-containing chalcogels can integrate (O=U=O)²⁺ into their structure matrix by ion-exchange. In addition, Riley et al. reported that unsaturated and coordinatively saturated sulfides of the colloidal surface of the amorphous chalcogel show the sorption of UO₂²⁺ via "—S···U⁶⁺O₂²⁺" covalent interactions.³³ Thus, one can surmise that chalcogels with alkali metal ions will provide an unprecedented synergy of ion exchange and "—S···U⁶⁺O₂²⁺" covalent interactions for the capture of $[O=U=O]^{2+}$ ions.³³ In addition, radioactive ^{134/137}Cs⁺ and ⁹⁰Sr²⁺, which are the fission products of uranium, can be separated by the ion-exchange mechanism.

Here, we report the synthesis of the potassium-tinmolybdenum-sulfide (KTMS) gel whose gelation requires cooperative redox reactions of the gel-forming constituents of Mo, Sn, and S. The KTMS gel is a tunable semiconductor that demonstrates its constituent nanoparticles' quantum confinement optical properties. With a combination of X-ray photoelectron spectroscopy (XPS), synchrotron X-ray pair distribution functions (PDF), X-ray absorption near edge structure (XANES), and extended X-ray absorption fine structure (EXAFS), we show that KTMS is X-ray amorphous, and its local structure is very complex which consists of $\mathrm{Mo^{V}_{2}(S_{2})_{6}}$ and $\mathrm{Mo^{IV}_{3}S(S_{2})_{6}}$ species and various Sn-S polyhedra. We also report that KTMS is an effective sorbent for radioactive Sr²⁺, Cs⁺, and UO₂²⁺ species. KTMS's random porosities, S–S bonding network, surface polarizability, and ionically bonded cations make it a unique sorbent for diverse radioactive Sr²⁺, Cs⁺, and UO₂²⁺ ions. Importantly, despite being amorphous, KTMS is a pioneering example, showing ion-exchange properties with chemically distinct metal cations.

EXPERIMENTAL METHODS

Chalcogel Synthesis. KTMS was synthesized by mixing solutions of $Sn(C_2H_3O_2)_2$ (0.3 mmol, 0.071 g), K_2S (0.6 mmol, 0.066 g), and $(NH_4)_2MoS_4$ (0.3 mmol, 0.078 g) at room temperature. More precisely, $Sn(C_2H_3O_2)_2$ and $(NH_4)_2MoS_4$ were dissolved separately in 0.5 mL of formamide, and K_2S was dissolved in 1.0 mL of formamide. Subsequently, the tin acetate solution was added slowly to the potassium sulfide solution and mixed together by gentle shaking. To this mixture, the solution of $(NH_4)_2MoS_4$ was added slowly with concurrent gentle shaking, and then the solutions were left undisturbed. The monolith wet-gels of KTMS formed in 1 day.

The solidified gels were then washed with ethanol and water in a ratio of 4:1 and then only with ethanol for 4 days to remove any unreacted byproducts. Following this procedure, the gel was left uncovered to dry for 24 h, yielding xerogels. For the fabrication of aerogels, the washed wet-gels were soaked in anhydrous ethanol for supercritical drying. To obtain the aerogel, a monolithic wet-gel of KTMS was dried by using $\rm CO_2$ at a supercritical temperature range of 36–39 °C and pressure of ~1400 psi using an Autosamdri–815B (Tousimis) instrument.

Adsorption Experiments. The sorption experiments for Cs⁺, Sr²⁺, and UO₂²⁺ were conducted using the batch method with deionized water (DIW). For the capture experiments, KTMS (0.020 g) was soaked in the solution and was mixed in the vials for up to 24 h with an end-to-end rotator. Subsequently, the mixed solution was centrifuged for about 1 h. The supernatant was collected using a micropipette after 1 h of centrifugation. The kinetics experiments were conducted using 1000 ppb of Cs⁺, Sr²⁺, and UO₂²⁺ in a time scale from 5 min to 24 h, while the capacity tests were conducted from 1 to 1000 ppm for Cs⁺ and UO₂²⁺ ions and 1 to 500 ppm for Sr²⁺, in DIW. All the measurements were replicated at least twice, and the average values were taken for the calculations.

Inductively Coupled Plasma-Mass Spectroscopy. The samples from kinetic experiments for UO₂²⁺, Cs⁺, and Sr²⁺ were measured by inductively coupled plasma-mass spectroscopy using a Bruker Varian MS-820 mass spectrometer.

X-ray Photoelectron Spectroscopy. Atomic compositions and valence band structures (VBS) of KTMS and strontium-adsorbed KTMS were investigated using a Physical Electronics Inc. Versaprobe III X-ray photoelectron spectrometer (XPS). Monochromatic Al-K α X-rays were focused on the sample with a 100 μ m diameter spot size at a power of 25 W. A low voltage (100 V) Ar ion beam and BaO electron neutralizer (1.3 V, 20 µA) were used in tandem to compensate for surface charging and all spectra were additionally shifted to match the adventitious carbon 1s peak with 284.8 eV. Elemental transitions were collected with an analyzer pass energy of 55 eV and a takeoff angle of 45°. Signals averaged over 2 scans, except for the VBS which averaged over 4 scans each. The operating pressure was $<5 \times 10^{-6}$ Pa. The system was calibrated to Ag and Au surfaces freshly sputtered by an Ar ion gun. All spectra were analyzed and fit using Multipeak version 9.6.0.15, made by Physical Electronics Inc. Shirley background spectra of the elemental transitions were subtracted from the raw signal, except for the VBS which was maintained with any background intact.

Synchrotron X-ray Pair Distribution Function. Synchrotron X-ray pair distribution function data were collected from the Advanced Photon Source (APS) of Argonne National Laboratory by the mail-in-ballot program using the 11-ID-B beamline at a wavelength of 0.1432 Å under ambient conditions. Prior to the experiment, the samples were ground to about the size of 50 μm and packed in a Kapton capillary. The rapid acquisition pair distribution function (RA-PDF) technique³⁸ was used to collect diffraction patterns at room temperature on powdered samples of KTMS. The data was integrated using the program Fit2D³⁹ and corrections (subtraction of background and container, Compton, and fluorescence scattering, geometric and adsorption correction, etc.)⁴⁰ were performed using the program PDFgetX3.⁴¹ The normalized data were truncated at 24 Å⁻¹ before the PDF calculation. PDFgui was used to model the data.⁴²

Synchrotron X-ray Absorption Spectroscopy. The pristine KTMS was analyzed by synchrotron X-ray absorption near edge structure (XANES) and extended X-ray absorption fine structure (EXAFS) for Mo and Sn K-edges. Mo K-edge XANES and EXAFS data were collected using the Canadian Light Source (CLS) Very Sensitive Elemental and Structural Probe Employing Radiation from a Synchrotron (VESPERS, 07B2-1) beamline (Saskatoon, SK, Canada). The VESPERS beamline is a hard X-ray microprobe beamline equipped with double crystal Si (111) and double multilayer monochromators. The double crystal Si (111) monochromator was used to scan the photon energy for Mo K-edge XANES and EXAFS measurements. The experiment was carried out using fluorescence

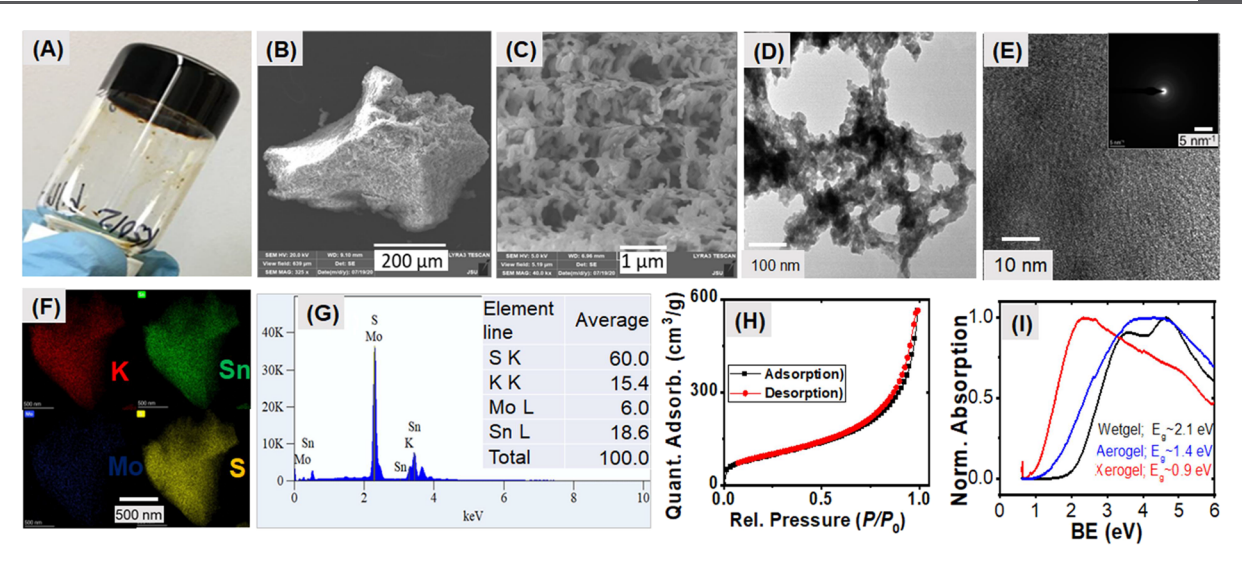


Figure 1. Photograph of the inverted vial shows the monolith wet-gel of KTMS (A); SEM images of aerogels confirming the homogeneity and porous nature of the gels (B–C); TEM image of the aerogels show the aggregation of the nanoparticles with meso to macroporosities (D); HRTEM showing no evidence of lattice fringe formation (E), inset in (E) shows SAED image reveals diffuse rings suggesting an amorphous structure; EDS elemental mapping and the spectrum showing the presence of K, Sn, Mo, and S (F–G); inset in (G) shows average chemical compositions; BET surface area revealed high surface area of the aerogels (H); solid-state UV/Vis absorption spectra demonstrate the three distinct optical band gap energies of the KTMS semiconductor (I).

mode, where the characteristic X-ray fluorescence Mo was collected by a four-element Vortex silicon drift detector and the incident flux by an N2-filled ionization chamber. Sn K-edge XANES and EXAFS data were collected using the CLS Biological X-ray Absorption Spectroscopy (BioXAS, 07ID-2) beamline. The BioXAS beamline is optimized for high sensitivity and high-resolution hard X-ray absorption spectroscopy experiments. A double crystal Si (220) monochromator was used to scan the photon energy in the vicinity of the Sn K absorption edge at 29,200 eV. Rh-coated toroidal mirrors performed the rejection of second and higher harmonics and moderate beam focusing down to $0.6 \times 2 \text{ mm}^2$ in the sample position with total flux in the order of 1012 photons/s. The experiment was carried out in the energy dispersive fluorescent mode, where the characteristic X-ray fluorescence from Sn was collected by a Canberra 32-element Ge detector and the incident by an N2-filled ionization chamber. The CLS storage ring was operated in the Top-Up mode with an electron current at ~200 mA during the measurements.

The EXAFS analysis was done using the entirely Python-based tool Larch, version 0.9.65, and the FEFF calculations were done by the FEFF 8L algorithm using the same software. For the EXAFS fitting for the Mo K-edge of the KTMS, the fitting range in k space was 2.00 to 9.70 Å⁻¹ with a k weighing of 2; for the fitting in r and real space, the range was 1.00 to 4.50 Å. Fourier transformation (FT) was done using the Kaiser-Bessel window at a dk value of 3.00 within the k value of 2.00 to 9.70 Å⁻¹. The χ^2 and reduced χ^2 values for the fitting are 22.293 and 3.621, respectively. EXAFS fitting of KTMS for the Sn Kedge was also performed using Larch. The fitting range in k space was 1.00 to 12.00 $\rm{\mathring{A}}^{-1}$ at a k weight of 2. The Kaiser-Bessel window at a $\rm{d}k$ value of 3.00 was used for the Fourier transformation. The fitting range in both r and real space was 0.0 to 6.0 Å. The χ^2 and reduced χ^2 values obtained from the fitting were 2.7388 and 0.0883, respectively. Background subtraction was carried out using the AUTOBK algorithm with an r-bkg value of 1.10 for both Mo and Sn K-edges EXAFS.

RESULTS AND DISCUSSION

Synthesis and Characterization. Black monolith wet-gel of potassium—tin—molybdenum—sulfide (KTMS) has been synthesized by mixing solutions of K_2S , $(NH_4)_2MoS_4$, and $Sn(CH_3COO)_2$ in formamide at ambient conditions (Figure 1A and details in the SI). The spongy aerogel of KTMS was

obtained by supercritical drying of its wet-gel. This process is necessary to deactivate the capillary forces of the nanopores and to retain the inherited porous features of the wet-gel in the aerogel without a significant volume loss (Figure 1). The gelforming particles are primarily on the nanometer (colloidal) scale and are formed by the covalent interactions of metalsulfide anionic clusters and tin cations to develop a bonding network of $(-Mo-S^{z-}-Sn-)_n \to \infty$ in space. The electrostatically bound K+ ions are plausibly distributed in the open pores of the covalent networks of $(-Mo-S^z-Sn-)_n \to \infty$. The atomic scale formation of KTMS leads to the primary particles which can subsequently be aggregated to form larger secondary particles following the chemistry of sol-gel synthesis. ^{23,43} An encapsulation of the primary particles, for instance, "K-Sn-Mo-S" for KTMS, with a solvent such as formamide, yields extremely small pores, while the encapsulation of the larger secondary particles yields larger pores ranging from meso (2-50 nm) to macropores (>50 nm).²³

Scanning electron microscopy (SEM) images show the homogeneity of the KTMS aerogel (Figure 1B, C). The gel particles consist of interlinked nanoparticle aggregates to yield a sponge-like material. The nanoparticles of the KTMS aerogel exhibit irregular sizes and shapes. Transmission electron microscopy (TEM/HRTEM) imaging shows that the aerogel materials consist of irregular nanoparticle aggregates (Figure 1D). The gel-forming particles are connected in a random fashion, leaving a percolated porous network. The pores are distributed randomly and do not seem to form regular channels throughout the aerogels (Figures 1B-D and S1). The TEM and HAADF-STEM images also show that the pore sizes vary from a few nanometers to several hundred nanometers, suggesting the presence of meso- and macroporosity around the agglomerated nanoparticles (Figures 1 and S1). However, the determination of the size of the particles in the KTMS aerogel was not possible mainly because of the agglomerated nature of the irregularly shaped and sized nanoparticles (Figure S1). High-resolution transmission electron microscopy (HRTEM) shows the absence of any

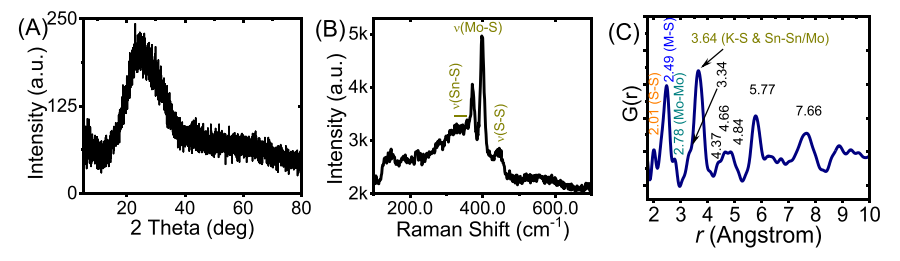


Figure 2. X-ray powder diffraction pattern of the KTMS xerogels (A), Raman shift shows evidence of the ν (Mo–S) and ν (S–S) vibration bands; the Sn–S vibration bands may be attributed to the hump in the 320–350 cm⁻¹ region (B), and the PDF of the KTMS shows the S–S, M–S (M = Mo and Sn), Mo–Mo and K–S correlations (C).

lattice fringes, suggesting the lack of the periodicity of the gels' matrix, which is relevant to amorphous structures (Figure 1E). Selected area electron diffraction (SAED) shows weakly intense diffused rings, suggesting the amorphous nature of the materials (Figure 1E, inset). Energy-dispersive X-ray spectroscopy (EDS) elemental mapping shows the presence of K, Sn, Mo, and S in the KTMS aerogel (Figure 1F). EDS analysis of the pristine KTMS aerogels also determined the average elemental abundances of K, Sn, Mo, and S atoms of 15.4, 18.6, 6.0, and 60.0%, respectively (Figure 1G).

Besides TEM and SEM, the internal porosity of the KTMS aerogel was further verified by N2 adsorption-desorption measurement at 77K (Figure 1H). This experiment revealed that the Brunauer-Emmett-Teller (BET) surface area of KTMS is 104.01 m²/g while the Langmuir and single point surface areas were obtained as 829.5 and 321.2 m²/g, respectively. The BET surface area of the KTMS aerogel is comparable to that of $Pt_{1.4}SnS_{4.0} \sim 108$ to 117 m²/g,⁴ thiostannate ammonium chalcogenide aerogel (TAC-4) ~ $158 \text{ m}^2/\text{g}$, ⁴⁴ Na-Mn-Sn-S (NMSC-1 and 2) ~ 95, and 124 m²/g. The presence of heavier atoms like Sn in these gels may be attributed to the relatively lower surface area compared with other chalcogels. This phenomenon was previously demonstrated for Mo₂Fe₆S₈-Sn₂S₆ chalcogels. ⁴⁵ Apart from this, condensation of the KTMS chalcogel particles during the supercritical drying process cannot be ruled out. In addition, BET revealed the adsorption and desorption average pore volume as 0.758 and 0.859 cm³/g which yielded the pore diameter of 29.16 and 33.02 nm, respectively following the equation $D_p = 4V_T/S_{BET}$, where D_p is pore diameter, V_T is adsorption/desorption pore volume (0.758 and 0.859 cm 3 /g, $S_{\rm BET} \sim 104.01$ m 2 /g). This indicated the presence of a typical mesoporosity for aerogels. The hysteresis loop was observed in the high-pressure regime. This may be due to the effects of pore blocking or capillary condensation. Thermogravimetric analysis shows the decomposition of KTMS after an initial loss of moisture (Figure S2).

The optical band gap of the KTMS wet-gel revealed that it is a medium band gap semiconductor with a band gap energy of \sim 2.1 eV (Figure 1I). The semiconducting property of the KTMS wet-gels is attributed to a greater overlapping of the atomic orbitals of the metals and sulfide ligands. After supercritical drying, the band gap of the aerogels became \sim 1.4 eV, while it further decreased to \sim 0.9 eV for the xerogels. A red shift of the band gap energy from the wet-gel \rightarrow aerogel \rightarrow xerogel is related to increased sizes of the nanoparticles. This is due to the condensation of KTMS's colloidal-sized particles of the wet-gel into larger particles for the aero- and xerogel, respectively. These features demonstrate the characteristic quantum-confined optical properties of the KTMS

nanoparticles, in agreement with that of chalcogenides-based aerogels. 4,5,48 TEM images show the interconnected nanoparticles of the aerogel and wet-gels; however, the particle size and morphology of the xerogel (Figure S1B) are distinctive to its wet- and aerogel counterparts, showing the condensation of the aggregated nanoparticles into larger particles with sizes of several hundred nanometers (Figure S3). The powder X-ray diffraction pattern of pristine KTMS xerogel revealed two relatively intense broad peaks at $2\theta \sim 20-30^{\circ}$ and two weaker and broad peaks at $2\theta \sim 50^{\circ}$ and 60° (Figure 2A). Such broad features of the X-ray diffraction patterns represent long-range disordered or essentially amorphous structures of the KTMS gels. Similarly, the XRD of the aerogel shows their amorphous characteristics, however, the supercritical drying condition (36–39 °C and 1400 psi) required to fabricate the aerogel may be attributed to a slight structural ordering, as seen in the XRD (Figure S4). The impact of such a structural ordering in band gap energies cannot be completely ruled out.

The Raman spectrum of pristine KTMS xerogel shows two intense peaks at 371 and 400 cm $^{-1}$, and several weaker peaks at 444, 220, 185, and 145 cm $^{-1}$ (Figure 2B). The peak at about 444 cm $^{-1}$ originates from the S–S vibrational energy, ⁴⁹ and the strong peaks at 371 and 400 cm $^{-1}$ may originate from the symmetric and asymmetric vibration of Mo–S bonding. ⁵⁰ The Sn–S vibrational bands may be hidden in the broad hump ranging from \sim 300–350 cm $^{-1}$ in the Raman spectrum. ⁵¹

To understand the local structure of amorphous KTMS, we conducted synchrotron X-ray pair distribution function (PDF) analysis using Argon National Laboratory's Advanced Photon Source (APS) (Figure 2C). PDF shows the atomic correlation up to ~10 Å which suggests a hierarchy in the atomic arrangement in its local structure. The lack of peaks beyond ~10 Å indicated the absence of long-range translational symmetry of KTMS as evidenced by XRD. Specifically, the PDF of KTMS revealed an atomic correlation of the peak at ~2.01 Å with the S-S bonding interaction of the $(S_n)^{2-}$ group,²⁴ which is consistent with Raman spectroscopy. The peak at \sim 2.49 Å can be attributed to the average M-S (M = Mo and Sn) bonding correlations, and the peak at 2.78 Å represents Mo-Mo distances. 14 Hence, Mo-Mo bonding correlation implied the presence of bi- or trinuclear clusters of Mo, similar to those in crystalline (NH₄)₂Mo₂(S₂)₆ and (NH₄)₂Mo₃S(S₂)₆. ⁵²⁻⁵⁴ Notably, despite the use of MoS₄²⁻ anions as a precursor for KTMS gels, it does not show the $d(Mo-S) \sim 2.2$ Å bonding correlation as observed for MoS_4^{2-} . A similar finding was also reported for $MoS_x^{-14,24}$ In addition, an intense band at ~ 3.3 Å may relate to the S····S correlation of metal sulfide in the first coordination sphere 12 while the strong peak centered at 3.7 Å can be attributed to the superimposed correlations for K····S and M····M (M = Mo and/or Sn) bonds.

X-ray photoelectron spectroscopy was conducted to understand the chemical states of the atoms on the surface of the KTMS gels (Figure 3). The bands at ~294.58 and 297.40 eV

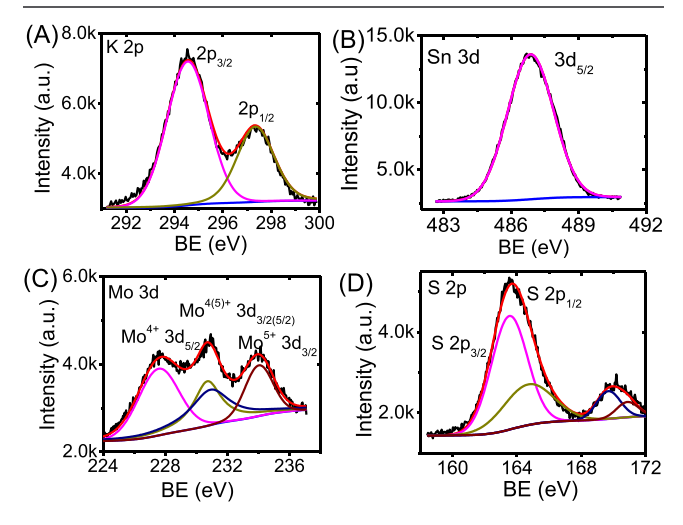


Figure 3. X-ray photoelectron spectra showing the K 2p (A), Sn 3d (B), Mo 3d (C), and S 2p (D) orbital excitation energies of the KTMS chalcogels.

correspond to $2p_{3/2}$ and $2p_{1/2}$ of K^+ , while the peak at 486.99 eV corresponds to the $3d_{5/2}$ binding energy of $5n^{4+}$. The bands at 227.69-234.10 eV were attributed to excitation energies of Mo 3d orbital. The deconvoluted peaks at 227.69 and 230.78 eV represent the orbital energies for $6n^{4+}$ 3d_{5/2} and 3d_{3/2}, and the peaks at 231.09 and 234.10 eV are attributed to $6n^{5+}$ 3d_{5/2} and 3d_{3/2}, respectively. Shows a $6n^{5+}$ 3d_{5/2} and 3d_{3/2}, respectively. Shows are consistent with the S 2p orbital excitation energy. Shows More precisely, the deconvoluted peaks at 161.86 and 162.95 eV may have originated from the sulfur $6n^{5+}$ 3d 3d 3d 2p_{1/2} of polysulfide species, while the broad peak at $6n^{5+}$ 3d 2p_{1/2} of polysulfide species, while the broad peak at $6n^{5+}$ 3d 2p_{1/2} of polysulfide species, while the broad peak at $6n^{5+}$ 3d 2p_{1/2} of polysulfide species, while the broad peak at $6n^{5+}$ 3d 2p_{1/2} of polysulfide species, while the broad peak at $6n^{5+}$ 3d 2p_{1/2} of polysulfide species, while the broad peak at $6n^{5+}$ 3d 2p_{1/2} of polysulfide species, while the broad peak at $6n^{5+}$ 3d 2p_{1/2} of polysulfide species, while the broad peak at $6n^{5+}$ 3d 2p_{1/2} of polysulfide species, while the broad peak at $6n^{5+}$ 3d 2p_{1/2} 3d 2p_{1/2}

To understand the chemical bonding and coordination environment further, we conducted synchrotron Mo and Sn K-edge X-ray absorption spectroscopy (XAS) investigations (Figures 4 and S5, and Table 1). Mo K-edge X-ray absorption

near edge structure (XANES) shows a broad absorption at 20031.4 eV (Figure 4A), which may suggest the presence of Mo ions with different oxidation states, as reported for amorphous MoS₃. The Sn K-edge XANES spectrum shows a prominent sharp peak at 29,206.6 eV, indicating the presence of Sn⁴⁺ (Figure 4D). Hence, the Mo and Sn K-edge XANES spectra of KTMS indicated the presence of the multivalent oxidation of Mo and the + IV oxidation state of Sn, consistent with the XPS results. It is worth mentioning that the oxidation of Sn²⁺ \rightarrow Sn⁴⁺ and sulfide (S²⁻) \rightarrow polysulfide (S_n²⁻, $n \ge 2$) is attributed to the reduction of Mo⁶⁺ center of [Mo^{VI}S₄]²⁻ to Mo^{5+/4+} as determined by the XPS and XANES analysis. Also, since the reaction was carried out at ambient conditions, the role of atmospheric oxygen and moisture for the oxidation of Sn²⁺ and S²⁻ cannot be ruled out.

From the fitting of the Mo K-edge extended X-ray absorption fine structure (EXAFS) spectrum, we have obtained Mo-S and Mo-Mo paths using molecular $(NH_4)_2Mo_2(S_2)_6$ and $(NH_4)_2Mo_3S(S_2)_6$ (Figure 4B, C and Table 1) as models. 52-54 The fitting of EXAFS revealed the presence of Mo-S interactions along with Mo-Mo dinuclear (Mo₂) and trinuclear (Mo₃) clusters that agree with the PDF (Figure 2C). This finding indicates that the local structure of KTMS contains structural features similar to both $[Mo_2(S_2)_6]^{2-}$ and $[Mo_3S(S_2)_6]^{2-}$. Since $S_2 = 10^{-52-54}$ Moreover, the fitting of the EXAFS data also revealed the Mo-S-S- paths. This is indicative of the intercluster connection through -S-S- covalent interactions. This observation is analogous to other chalcogels, namely, $Mo_3S(S_2)_6$ type clusters containing $MoS_{x}^{-14,24}$ Importantly, unlike previous reports, ^{14,24} KTMS shows the presence of both dinuclear (Mo₂) and trinuclear (Mo₃) clusters. The Sn K-edge EXAFS spectrum of the KTMS gel showed the presence of multiple Sn-S geometries (Figure 4E, F). The fitting of the Sn K-edge EXAFS data with a Sn-S path at ~2.22 Å using a reference compound of Na₄SnS₄⁶⁰ demonstrated the presence of the tetrahedral Sn-S system while the Sn-S path at ~2.40 Å from SnS₂ 61 as reference shows the presence of an octahedral Sn-S geometry. At higher r in the EXAFS, the r space data fitting yielded Sn-Sn contributions similar to Na₄Sn₃S₈ that possesses tetrahedral and trigonal bipyramidal Sn-S coordination polyhedra. 62 All these structural features suggest that KTMS possesses a very complex structure with

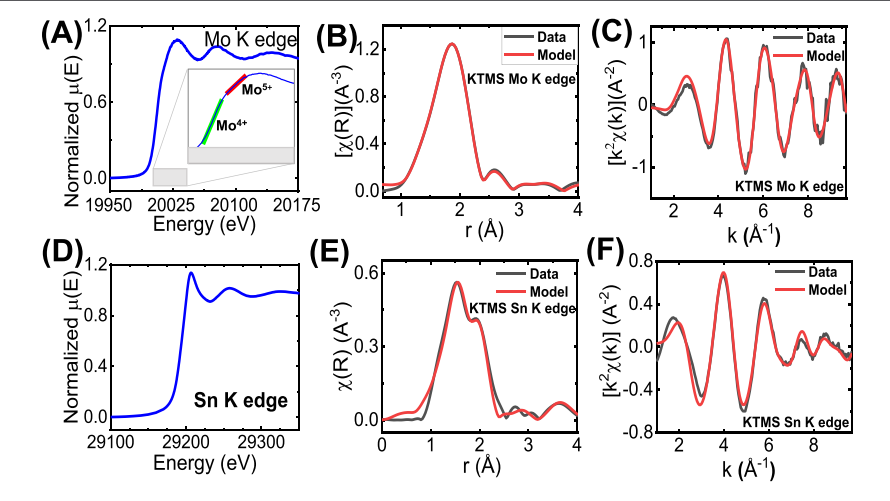


Figure 4. Top panel: Mo K-edge XANES spectrum (A) of KTMS and its EXAFS spectra at R space (B), k space (C); bottom panel: Sn K-edge XANES spectrum (D) of KTMS and its EXAFS spectra at R space (E), k space (F).

Table 1. EXAFS Fitting Parameters of Mo and Sn K Edges of the KTMS Aerogel^a

path	ref.	$r_{\rm eff}$ (Å)	R (Å)	N	ΔE_0 (eV)	DWF, σ^2 (Å ²)	R factor
$Mo^{IV}-S_1$	$Mo_3S_{13}^{2-54}$	2.35	1.97 (±0.011)	4	$-8.09 (\pm 0.78)$	0.032 (±0.002)	0.0009
$Mo^V - S_2$	$Mo_2S_{12}^{2-53,64}$	2.46	$2.30 \ (\pm 0.008)$	6		$0.008 \ (\pm 0.002)$	
Mo^V $-Mo^V$	$Mo_2S_{12}^{2-53,64}$	2.83	$2.63 (\pm 0.012)$	4		$0.009 (\pm 0.002)$	
Mo^{IV} $-Mo^{IV}$	$Mo_3S_{13}^{2-54}$	2.72	$2.45 \ (\pm 0.008)$	3		$0.002 (\pm 0.001)$	
$Mo^V - S_3$	$Mo_2S_{12}^{2-53,64}$	4.77	$4.97 (\pm 0.021)$	4		$0.007 (\pm 0.003)$	
$Mo^{IV}-S_4$	$Mo_3S_{13}^{2-54}$	4.22	4.22 (fix)	3		0.010 (fix)	
$Sn^{IV}-S$	SnS_4^{4-60}	2.43	$2.2168(\pm0.0078)$	4	$-2.09 (\pm 0.79)$	$0.0051(\pm0.0011)$	0.0326
$Sn^{IV}-S$	SnS_2^{61}	2.60	$2.4048(\pm0.0079)$	6		$0.0059(\pm0.0010)$	
$Sn^{IV}-Sn^{IV}$	$Sn_3S_8^{4-62}$	4.01	$4.0165(\pm0.0247)$	3		$0.0091(\pm 0.0028)$	
$Sn^{IV}-Sn^{IV}$	$Sn_3S_8^{4-62}$	3.65	$3.5296(\pm0.0632)$	4		$0.0229(\pm0.0088)$	
$Sn^{IV}-Sn^{IV}$	$Sn_3S_8^{4-62}$	3.71	$3.2106(\pm0.0438)$	4		$0.0221(\pm 0.0061)$	

 a r_{eff} (Å) = bond distance from the reference crystal structure, R (Å) = bond distance after feff fitting, N = coordination number, ΔE_{0} = energy shift, and DWF = Debye—Waller factor.

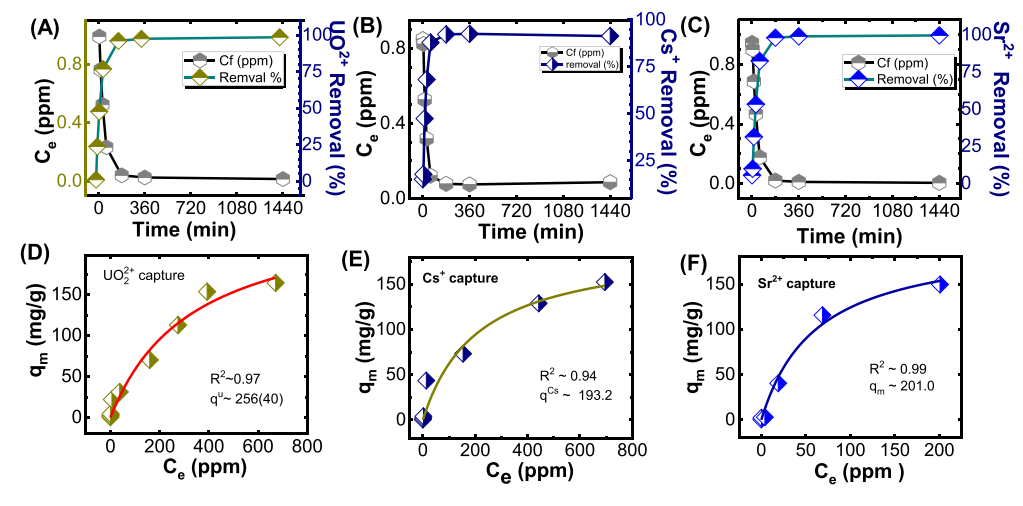


Figure 5. Sorption kinetics and capacities of KTMS for UO_2^{2+} (A,D), Cs^+ (B,E), and Sr^{2+} (C,F) from DIW, using 20 mg of sorbent in 10 mL of DIW solutions.

various coordination polyhedra which may be due to the trapping of the metastable phase in a local minimum of the energy landscape. It is worth mentioning that although the reference compounds used for the EXAFS data fitting may not represent the exact atomic environment of the amorphous KTMS, the fitting of the EXAFS data and the FEFF paths⁶³ provide a plausible local atomic arrangement that integrates $Mo_2(S_2)_6$ and $Mo_3S(S_2)_6$ structural moieties for molybdenum and a coordination feature related to Na₄Sn₃S₈ and SnS_2 . $^{52-54,60,61}$ Despite this finding, the actual coordination environment of the amorphous KTMS may be more complex. Understanding the structure of amorphous materials is bottlenecked because of the available method to determine their structures, especially for such a complex quaternary system, which lacks a representative model of crystalline compounds.

Removal of UO₂²⁺, Cs⁺, and Sr²⁺ with KTMS. We investigated the KTMS aerogel for the sorption of UO_2^{2+} , Cs^+ , and Sr^{2+} from aqueous solutions (Figure 5). A kinetic study shows that KTMS achieved ~96.0, 92.2, and 98.0% removal for UO_2^{2+} , Cs^+ , and Sr^{2+} , respectively, from 1000 ppb spiked solutions after 3 h (Figure 5 and Tables S1–S3). For UO_2^{2+} and Sr^{2+} , the removal percentage slowly increased to 98.9% and 99.6% in 24 h, leaving residual concentrations of ~15 and 4 ppb, respectively. These results suggest that KTMS is an efficient sorbent for the removal of uranium and strontium

from water. Our experiments also revealed the distribution $\begin{pmatrix} c_0 - c_c \end{pmatrix}_{V,V}$

constants, $K_d = \frac{\left(\frac{C_0-e}{C_c}\right) \times V}{m}$, where C_0 and C_e are the initial and final concentrations; "V" is the volume of solution and "m" is the mass of sorbent, are 4.6×10^4 , 5.3×10^3 , and 1.2×10^5 mL/g for UO₂²⁺, Cs⁺, and Sr²⁺, respectively. Notably, the distribution constants for UO₂²⁺ and Sr²⁺ were $\geq 10^4$ mL/g, suggesting a higher affinity of KTMS to these radioactive species. 36,55,65

To assess the uptake capacity and adsorption isotherm, we investigated the sorption of UO_2^{2+} , Cs^+ , and Sr^{2+} for a broad range of concentrations (Figure 5D–F and Tables S4–S6). These experiments revealed that the sorption capacity increased with the increase in concentrations of UO_2^{2+} , Cs^+ , and Sr^{2+} until an equilibrium was reached (Tables S4–S6). The experimental isotherm data were fitted using the Langmuir isotherm model which predicts adsorbate moieties undergo monolayer type coverage on the surface of the adsorbent. This model predicts that once an adsorption site is occupied, no further adsorption can occur at the same site. The Langmuir isotherm model is shown in eq 1:

$$q = q_{\rm m} \frac{bC_{\rm e}}{1 + bC_{\rm e}} \tag{1}$$

where C_e (ppm) is the concentration at equilibrium, q (mg/g) is the equilibrium sorption capacity of the adsorbed UO_2^{2+} ,

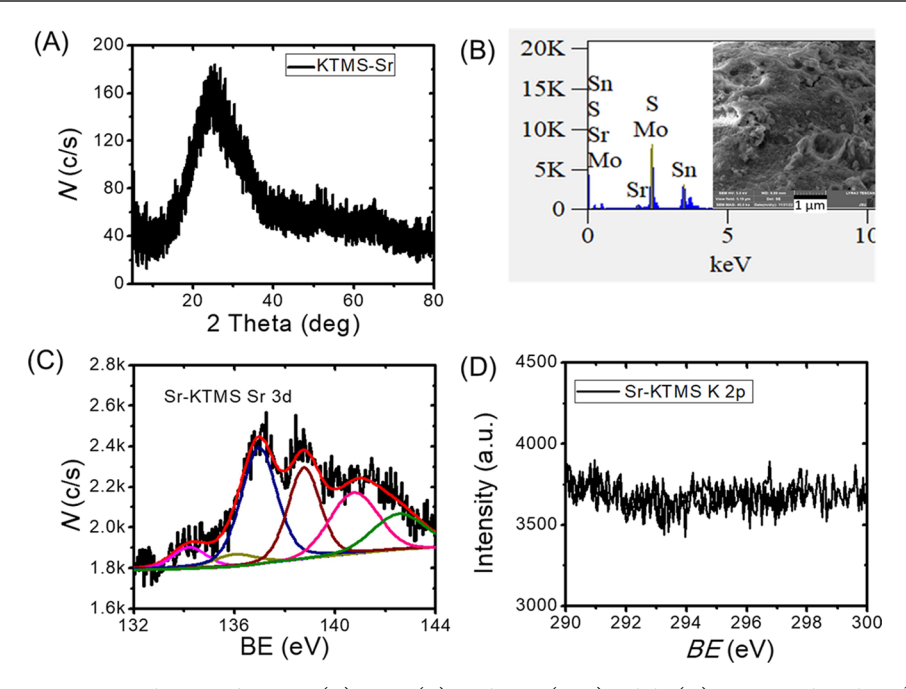


Figure 6. Analysis of the post interacted KTMS by XRD (A), EDS (B), and XPS (C,D); while (C) is assigned as the Sr^{2+} 3d orbital energy, the region of the K 2p energy shows the absence of K^+ ions suggesting the ion-exchange of the K^+ ions by Sr^{2+} in the KTMS chalcogel particles.

Table 2. Chalcogenide-Based Gels and Their Interactions with Metal Cations

chalcogel	physical state	interacting ions	capacity, $q_{\rm m}$, $({\rm mg/g})$	$K_{\rm d}~({\rm mL/g})$	sorption process	ref
KTMS	amorphous	Cs ⁺	~152	$\sim 5.3 \times 10^3$	ion-exchange	this worl
		Sr ²⁺	~142	$\sim 1.2 \times 10^5$		
		UO_{2}^{2+}	~164	$\sim 4.6 \times 10^4$		
NMSC ^a	crystalline	Cs^+	~78	$\sim 8.83 \times 10^2$	ion-exchange	1
		Sr ²⁺	~41	$\sim 4.36 \times 10^2$		
TAC-3 ^b	amorphous	Cs^+	~191.1	$\sim 3.48 \times 10^3$	ion-exchange	44
$(NH_4)_{0.2}MoS_x$	amorphous	K ⁺	-	-	ion-exchange	14
		Cs ⁺				
KCo ₆ S ₂₁	nanocrystalline	K ⁺	-	-	ion-exchange	34
ZnS	nanocrystalline	$Pb^{2+} Hg^{2+}$	~2127	$\sim 5.0 \times 10^4$	ion-exchange	13
			~1769.9	$\sim 1.95 \times 10^5$		
$ZnSnS_x$ (ZTS-cg3)	amorphous	Hg^{2+}	~1119.9	$\sim 1.1 \times 10^{8}$	ion-exchange	17
		Pb^{2+}	~1116.8	$\sim 8.5 \times 10^5$		
		Cd^{2+}	~1057.8	$\sim 4.8 \times 10^{8}$		
		Cu ²⁺	~854.8	$\sim 1.0 \times 10^5$		
		Zn^{2+} Fe ²⁺	~895.0	$\sim 3.98 \times 10^5$		
			~ 62.0	$\sim 7.05 \times 10^3$		
CoBiMoS	amorphous	UO_{2}^{2+}	-	$\sim 1.81 \times 10^3$	surface sorption	33
CoCrMoS	amorphous	UO_2^{2+}	-	$\sim 3.15 \times 10^2$	surface sorption	33
CoNiMoS	amorphous	UO_2^{2+}	-	$\sim 8.08 \times 10^{2}$	surface sorption	33
PtGeS	amorphous	UO_2^{2+}	-	$\sim 9.43 \times 10^4$	surface sorption	33
SnS	amorphous	UO ₂ ²⁺	-	$\sim 2.31 \times 10^4$	surface sorption	33

^aNa-Mn-Sn-S chalcogel. ^bTin ammonium chalcogel with methylammonium, TAC-3.

Cs⁺, and Sr²⁺, $q_{\rm m}$ (mg/g) is the theoretical maximum sorption capacity, b (L·mg⁻¹) is the Langmuir constant. Hence, the maximum adsorption capacities, $(q_{\rm m})$, obtained from Langmuir fitting were 256 (±40) mg/g (R^2 = 0.97) for UO₂²⁺, 193(±38) mg/g (R^2 = 0.94) for Cs⁺, and 200(±19) mg/g (R^2 = 0.99) for Sr²⁺. These values of $q_{\rm m}$ are close to the experimental values within the range of standard deviation (Tables S4–S6). Such high correlation coefficients suggest a good fitting with the Langmuir model. The Langmuir constant, b (L/mg), was 0.005(0) for UO₂²⁺, 0.003(3) for Cs⁺, and 0.016(4) for Sr²⁺. These values suggest that KTMS has a comparable affinity

toward the adsorbate ions. These suggest that KTMS is the unique example of an individual chalcogel that shows the sorption of chemically diverse cations of UO_2^{2+} , Cs^+ , and Sr^{2+} .

The xerogels of KTMS were prepared by drying the wet-gels at room temperature and pressure. This led to negligible pore densities across the gel matrix compared with aerogels, as seen from TEM (Figure S1). This resulted in significantly low sorption efficiencies of UO_2^{2+} , Cs^+ , and Sr^{2+} compared with aerogels. For example, the xerogel samples showed that the removal of UO_2^{2+} , Cs^+ , and Sr^{2+} from 100 ppm solutions is \sim 21.0, 10.3, and 21.1% while the aerogel showed 62.47, 86.98,

and 80.95%, respectively. These results suggest the importance of the porosities in the KTMS gels to facilitate the cation exchange. This finding is aligned with the previous finding by Brock and Coworkers and Riley et al., 13,66 where they independently verified the importance of the porosities to the cation exchange and noted that despite the presence of some porosities in the xerogels they behave more like dense solids matrix, limiting the diffusion of the exchangeable cations and the ion exchange become limited only to the surface of the particles.

Understanding the Sorption Properties of the K-Sn-Mo-S Chalcogel. We investigated the KTMS after the interactions with UO22+, Cs+, and Sr2+ ions by XRD, SEM, EDS, and FTIR (Figures 6 and S6, S7). The XRD of each sample shows broad featureless humps analogous to those of the pristine amorphous KTMS solids. SEM images displayed no significant changes in the morphology among KTMS gels after interacting with UO₂²⁺, Cs⁺, and Sr²⁺ ions. The EDS data of the KTMS treated with 5 mM Cs⁺, Sr²⁺, and UO₂²⁺ solutions show a complete removal of K+ ion demonstrating a complete exchange of the K⁺ by Cs⁺, Sr²⁺, and UO₂²⁺ (Figure S6). The sorption of Cs⁺ and Sr²⁺ can be attributed to the exchange of K⁺ ions by Cs⁺ and Sr²⁺. The XPS spectrum of the Sr²⁺ interacted KTMS shows the presence of Sr along with the Sn, Mo, and S but the absence of K+ (Figure 6), also confirming the ion-exchange mechanism for Sr²⁺.

The ion-exchange properties for amorphous chalcogel have been shown for $(NH_4)_{0.02}MoS_x$, where traces of electrostatically bound NH_4^+ (0.02 mol/formula unit) were exchanged by K^+ and Cs^+ ions. 14 Besides, K^+ ions of the nanocrystalline aerogels KCo_6S_{21} was exchanged by Cs^+ . Hence, our results suggest that despite being amorphous, KTMS possesses ion-exchange properties for both the mono- and divalent alkali metal cations, here Cs^+ and Sr^{2+} . Also, nanocrystalline NMSC shows the ion exchange properties for Sr^{2+} , however, KTMS pioneers the removal of Sr^{2+} ions as an amorphous chalcogel. A detailed list of chalcogels, their chemical states, and sorption mechanisms for UO_2^{2+} , Cs^+ , and Sr^{2+} are given in Table 2.

The infrared spectra of the pristine and the 5 mM of UO₂²⁺, Cs⁺, and Sr²⁺ solution-treated KTMS show a strong peak at \sim 918 cm⁻¹ only for the UO₂²⁺ interacted KTMS sample (Figure S7). The peak at 918 cm⁻¹ can be attributed to UO₂²⁺ vibrational energy as analogous to the previously reported UO₂²⁺ sorbed crystalline layered $K_{2x}Sn_{4-x}S_{8-x}$. So, 67 Besides EDS, this may further suggest a complete removal of K⁺ ions by UO_2^{2+} , where its linear geometry as $[O=U^{6+}=O]^{2+}$ may facilitate the ion exchange. This kind of ion-exchange property of $[O=U^{6+}=O]^{2+}$ is well-known for crystalline open frameworks and layered metal sulfides, 68 but to the best of our knowledge KTMS is the first example of an amorphous chalcogel to show ion exchange with UO₂²⁺. In addition, Riley et al., 33 reported the removal of UO_2^{2+} by CoMMoS (M = Cr, Ni, Bi), PtGeS, and SnS chalcogels, where the author demonstrated that a covalent interaction of the surface sulfides of the chalcogels and U^{6+} of the $UO_2^{\ 2+}$ ions, as in "-S··· $U^{6+}O_2^{2+n}$ attribute to the sorption of uranium from solutions. Consequently, one may surmise that KTMS attributes both ion exchange and surface sorption to sequester UO22+ from water. Thus, the structure of the KTMS may be deteriorated by the interactions with UO22+. In addition, during the batch experiment processes, surface sulfides may get oxidized due to the prolonged exposures of the chalcogels' nanoparticles in Cs⁺, Sr²⁺, and UO₂²⁺containing solutions. This interaction may

degrade the structure of KTMS. Overall, our results revealed KTMS as an efficient sorbent of chemically distinct UO_2^{2+} , Cs^+ , and Sr^{2+} . This, along with their facile room temperature and scalable synthesis, makes this material promising for the separation of radionuclides from spent nuclear fuels, defense legacy nuclear waste, and the extraction of uranium from water.

■ SUMMARY AND OUTLOOK

We have demonstrated the stabilization of a statically bound cation, K⁺, in the covalent network of Sn-Mo-S using a facile solution-processable synthesis at room temperature. Synchrotron X-ray PDF and XAS indicate a very complex local structure of KTMS that is plausibly related to crystalline molecular $Mo_2(S_2)_6$ and $Mo_3S(S_2)_6$ ions for molybdenum sites, while the Sn sites exhibit the Sn–S coordination similar to SnS_2 and $\text{Na}_4\text{Sn}_3\text{S}_8$. S2–54,60,61 We also show that KTMS efficiently removes UO₂²⁺, Sr²⁺, and Cs⁺ from the ppm to ppb levels. The sequestration of Sr²⁺ and Cs⁺ mainly occurs through ion-exchange of $K^{\scriptscriptstyle +}$ ions, while $UO_2^{\ 2^{\scriptscriptstyle +}}$ removal can be attributed to both the ion exchange of K⁺ by [O=U⁶⁺=O]²⁺ and covalent interactions between the surface sulfides of chalcogel particles and UO_2^{2+} , as in $S^{n-}\cdots UO_2^{2+}$ ($n \sim -1, -2$). These findings reveal KTMS as a pioneering example of a single chalcogel platform for the sequestration of chemically diverse radioactive species such as UO22+, Cs+, and Sr2+. Overall, the presence of electrostatically bound K⁺ ions in the covalent work of Sn-Mo-S and the strong Lewis acid-base interactions of the (poly)sulfide backbone of KTMS with UO22+, Cs+, and Sr2+ make KTMS an exceptional adsorbent for distinctive radioactive ions. This finding opens a new paradigm to design and develop new chalcogels with superior and multimodal sorption properties for chemically diverse radio-

ASSOCIATED CONTENT

Supporting Information

The Supporting Information is available free of charge at https://pubs.acs.org/doi/10.1021/acs.chemmater.3c01675.

Experimental details; TEM, HAADF-STEM, EXAFS analysis; PXRD, and FT-IR analysis of postinteracted KTMS aerogel; time-dependent and concentration-dependent sorption analysis of $\rm UO_2^{2+}$, $\rm Sr^{2+}$, and $\rm Cs^+$ (PDF)

AUTHOR INFORMATION

Corresponding Author

Saiful M. Islam — Department of Chemistry, Physics, and Atmospheric Sciences, Jackson State University, Jackson, Mississippi 39217, United States; oorcid.org/0000-0001-8518-1856; Email: Muhammad.s.islam@jsums.edu

Authors

Alicia Blanton — CSET/Environmental Science PhD Program and Department of Chemistry, Physics, and Atmospheric Sciences, Jackson State University, Jackson, Mississippi 39217, United States

Taohedul Islam – Department of Chemistry, Physics, and Atmospheric Sciences, Jackson State University, Jackson, Mississippi 39217, United States

Subrata Chandra Roy — Department of Chemistry, Physics, and Atmospheric Sciences, Jackson State University, Jackson, Mississippi 39217, United States

- Ahmet Celik Department of Chemistry, Physics, and Atmospheric Sciences, Jackson State University, Jackson, Mississippi 39217, United States
- Jing Nie Department of Chemistry, Physics, and Atmospheric Sciences, Jackson State University, Jackson, Mississippi 39217, United States
- David R. Baker Army Research Directorate, U.S. Army Research Laboratory, Adelphi, Maryland 20783, United States; Occid.org/0000-0002-9930-5183
- Dien Li Savannah River National Laboratory, Aiken, South Carolina 29808, United States
- Kathryn Taylor-Pashow Savannah River National Laboratory, Aiken, South Carolina 29808, United States; orcid.org/0000-0002-1986-0866
- Xianchun Zhu Department of Civil Engineering, Jackson State University, Jackson, Mississippi 39217, United States Avijit Pramanik — Department of Chemistry, Physics, and Atmospheric Sciences Leckson State University Leckson

Atmospheric Sciences, Jackson State University, Jackson, Mississippi 39217, United States; orcid.org/0000-0002-4623-2099

- Ruhul Amin Electrification & Energy Infrastructure Division, Oak Ridge National Laboratory, Oak Ridge, Tennessee TN-37830, United States; ⊚ orcid.org/0000-0002-0054-3510
- Renfei Feng Canadian Light Source, Saskatoon, Saskatchewan S7N 2 V3, Canada; oorcid.org/0000-0001-8566-4161
- Roman Chernikov Canadian Light Source, Saskatoon, Saskatchewan S7N 2 V3, Canada

Complete contact information is available at: https://pubs.acs.org/10.1021/acs.chemmater.3c01675

Author Contributions

The manuscript was written through the contributions of all authors. All authors have given approval to the final version of the manuscript.

Funding

US Department of Energy Minority Serving Institution Partnership Program (MSIPP) managed by the Savannah River National Laboratory under BSRA contract (RFP No. 0000542525 and 0000458357) U.S. Department of Energy (DOE) Office of Science User Facility operated for the DOE Office of Science by Argonne National Laboratory under Contract No. DE-AC02-06CH11357. United States Department of Education- Title III Institutional Aid Jackson State University-Historically Black Graduate Institutions (HBGI) Program 2019–2024 NSF Division of Chemistry (NSF-2100797) National Science Foundation, Grant ECCS-2025064 NIH grant: 1U54MD015929.

Notes

The authors declare no competing financial interest.

ACKNOWLEDGMENTS

This work was supported by the US Department of Energy Minority Serving Institution Partnership Program (MSIPP) managed by the Savannah River National Laboratory under BSRA contract (RFP No. 0000542525 and 0000458357) and United States Department of Education- Title III Institutional Aid Jackson State University-Historically Black Graduate Institutions (HBGI) Program —2019-2024 HBGI Activity: Strengthening the Environmental Science Ph.D. Program. SCR is thankful to the NSF Division of Chemistry (NSF-2100797).

All the ICP-MS analyses were conducted at JSU's core research centers supported by RCMI (NIH grant: 1U54MD015929). We also thank Dr. Matthew Newville (UChicago) for the advice about the fitting of the XAFS data. This research used resources from the Advanced Photon Source, a U.S. Department of Energy (DOE) Office of Science User Facility operated for the DOE Office of Science by Argonne National Laboratory under Contract No. DE-AC02-06CH11357. The mail-in program at Beamline 11-ID-B contributed to the data. X-ray absorption spectroscopy measurements were performed at the VESPERS and BioXAS beamlines, Canadian Light Source, which is supported by the Canada Foundation for Innovation (CFI), the Natural Sciences and Engineering Research Council (NSERC), the National Research Council (NRC), the Canadian Institutes of Health Research (CIHR), the Government of Saskatchewan, and the University of Saskatchewan. Any use of trade, firm, or product names is for descriptive purposes only and does not imply endorsement by the U.S. Government. TEM data was collected at the Chapel Hill Analytical and Nanofabrication Laboratory, CHANL, a member of the North Carolina Research Triangle Nanotechnology Network, RTNN, which is supported by the National Science Foundation, Grant ECCS-2025064, as part of the National Nanotechnology Coordinated Infrastructure, NNCI.

REFERENCES

ı

- (1) Ha, T. D. C.; Lee, H.; Kang, Y. K.; Ahn, K.; Jin, H. M.; Chung, I.; Kang, B.; Oh, Y.; Kim, M.-G. Multiscale Structural Control of Thiostannate Chalcogels with Two-Dimensional Crystalline Constituents. *Nat. Commun.* **2022**, *13* (1), 7876.
- (2) Shan, X.; Liu, J.; Mu, H.; Xiao, Y.; Mei, B.; Liu, W.; Lin, G.; Jiang, Z.; Wen, L.; Jiang, L. An Engineered Superhydrophilic/Superaerophobic Electrocatalyst Composed of the Supported CoMoS_x Chalcogel for Overall Water Splitting. *Angew. Chem., Int. Ed.* **2020**, 59 (4), 1659–1665.
- (3) Yang, L.; Liu, J. Amorphous Chalcogels with Local Crystallinity. *Nat. Commun.* **2022**, *13* (1), 7875.
- (4) Bag, S.; Trikalitis, P. N.; Chupas, P. J.; Armatas, G. S.; Kanatzidis, M. G. Porous Semiconducting Gels and Aerogels from Chalcogenide Clusters. *Science* **2007**, *317* (5837), 490–493.
- (5) Mohanan, J. L.; Arachchige, I. U.; Brock, S. L. Porous Semiconductor Chalcogenide Aerogels. *Science* **2005**, *307* (5708), 397–400.
- (6) Bag, S.; Arachchige, I. U.; Kanatzidis, M. G. Aerogels from Metal Chalcogenides and Their Emerging Unique Properties. *J. Mater. Chem.* **2008**, *18* (31), 3628–3632.
- (7) Yuhas, B. D.; Prasittichai, C.; Hupp, J. T.; Kanatzidis, M. G. Enhanced Electrocatalytic Reduction of CO₂ with Ternary Ni-Fe₄S₄ and Co-Fe₄S₄-Based Biomimetic Chalcogels. *J. Am. Chem. Soc.* **2011**, 133 (40), 15854–15857.
- (8) Yuhas, B. D.; Smeigh, A. L.; Samuel, A. P. S.; Shim, Y.; Bag, S.; Douvalis, A. P.; Wasielewski, M. R.; Kanatzidis, M. G. Biomimetic Multifunctional Porous Chalcogels as Solar Fuel Catalysts. *J. Am. Chem. Soc.* **2011**, *133* (19), 7252–7255.
- (9) Shim, Y.; Young, R. M.; Douvalis, A. P.; Dyar, S. M.; Yuhas, B. D.; Bakas, T.; Wasielewski, M. R.; Kanatzidis, M. G. Enhanced Photochemical Hydrogen Evolution from Fe_44S_4 -Based Biomimetic Chalcogels Containing M^{2+} (M = Pt, Zn, Co, Ni, Sn) Centers. *J. Am. Chem. Soc.* **2014**, *136* (38), 13371–13380.
- (10) Shim, Y.; Yuhas, B. D.; Dyar, S. M.; Smeigh, A. L.; Douvalis, A. P.; Wasielewski, M. R.; Kanatzidis, M. G. Tunable Biomimetic Chalcogels with Fe₄S₄ Cores and $[Sn_nS_2]^{n+2}$ $[sn_nS_2]^{n+2}$ Building Blocks for Solar Fuel Catalysis. *J. Am. Chem. Soc.* **2013**, *135* (6), 2330–2337.

- (11) Doan-Nguyen, V. V. T.; Subrahmanyam, K. S.; Butala, M. M.; Gerbec, J. A.; Islam, S. M.; Kanipe, K. N.; Wilson, C. E.; Balasubramanian, M.; Wiaderek, K. M.; Borkiewicz, O. J.; Chapman, K. W.; Chupas, P. J.; Moskovits, M.; Dunn, B. S.; Kanatzidis, M. G.; Seshadri, R. Molybdenum Polysulfide Chalcogels as High-Capacity, Anion-Redox-Driven Electrode Materials for Li-Ion Batteries. *Chem. Mater.* **2016**, 28 (22), 8357–8365.
- (12) Bag, S.; Gaudette, A. F.; Bussell, M. E.; Kanatzidis, M. G. Spongy Chalcogels of Non-Platinum Metals Act as Effective Hydrodesulfurization Catalysts. *Nat. Chem.* **2009**, *1* (3), 217–224.
- (13) Pala, I. R.; Brock, S. L. ZnS Nanoparticle Gels for Remediation of Pb²⁺ and Hg²⁺ Polluted Water. *ACS Appl. Mater. Interfaces* **2012**, *4* (4), 2160–2167.
- (14) Subrahmanyam, K. S.; Malliakas, C. D.; Sarma, D.; Armatas, G. S.; Wu, J.; Kanatzidis, M. G. Ion-Exchangeable Molybdenum Sulfide Porous Chalcogel: Gas Adsorption and Capture of Iodine and Mercury. J. Am. Chem. Soc. 2015, 137 (43), 13943–13948.
- (15) Subrahmanyam, K. S.; Sarma, D.; Malliakas, C. D.; Polychronopoulou, K.; Riley, B. J.; Pierce, D. A.; Chun, J.; Kanatzidis, M. G. Chalcogenide Aerogels as Sorbents for Radioactive Iodine. *Chem. Mater.* **2015**, *27* (7), 2619–2626.
- (16) Subrahmanyam, K. S.; Spanopoulos, I.; Chun, J.; Riley, B. J.; Thallapally, P. K.; Trikalitis, P. N.; Kanatzidis, M. G. Chalcogenide Aerogels as Sorbents for Noble Gases (Xe, Kr). *ACS Appl. Mater. Interfaces* **2017**, *9* (39), 33389–33394.
- (17) Oh, Y.; Bag, S.; Malliakas, C. D.; Kanatzidis, M. G. Selective Surfaces: High-Surface-Area Zinc Tin Sulfide Chalcogels. *Chem. Mater.* **2011**, 23 (9), 2447–2456.
- (18) Riley, B. J.; Chun, J.; Ryan, J. V.; Matyáš, J.; Li, X. S.; Matson, D. W.; Sundaram, S. K.; Strachan, D. M.; Vienna, J. D. Chalcogen-Based Aerogels as a Multifunctional Platform for Remediation of Radioactive Iodine. *RSC Adv.* **2011**, *1* (9), 1704–1715.
- (19) Mohanan, J. L.; Brock, S. L. A New Addition to the Aerogel Community: Unsupported CdS Aerogels with Tunable Optical Properties. *J. Non-Cryst. Solids* **2004**, *350*, 1–8.
- (20) Shafaei-Fallah, M.; He, J.; Rothenberger, A.; Kanatzidis, M. G. Ion-Exchangeable Cobalt Polysulfide Chalcogel. *J. Am. Chem. Soc.* **2011**, *1*33 (5), 1200–1202.
- (21) Bag, S.; Kanatzidis, M. G. Importance of Solution Equilibria in the Directed Assembly of Metal Chalcogenide Mesostructures. *J. Am. Chem. Soc.* **2008**, *130* (26), 8366–8376.
- (22) Polychronopoulou, K.; Malliakas, C. D.; He, J.; Kanatzidis, M. G. Selective Surfaces: Quaternary Co(Ni)MoS-Based Chalcogels with Divalent (Pb²⁺, Cd²⁺, Pd²⁺) and Trivalent (Cr³⁺, Bi³⁺) Metals for Gas Separation. *Chem. Mater.* **2012**, 24 (17), 3380–3392.
- (23) Bag, S.; Kanatzidis, M. G. Chalcogels: Porous Metal—Chalcogenide Networks from Main-Group Metal Ions. Effect of Surface Polarizability on Selectivity in Gas Separation. *J. Am. Chem. Soc.* **2010**, *1*32 (42), 14951–14959.
- (24) Staszak-Jirkovský, J.; Malliakas, C. D.; Lopes, P. P.; Danilovic, N.; Kota, S. S.; Chang, K.-C.; Genorio, B.; Strmcnik, D.; Stamenkovic, V. R.; Kanatzidis, M. G.; Markovic, N. M. Design of Active and Stable Co–Mo–S_x Chalcogels as pH-Universal Catalysts for the Hydrogen Evolution Reaction. *Nat. Mater.* **2016**, *15* (2), 197–203.
- (25) Subrahmanyam, K. S.; Malliakas, C. D.; Islam, S. M.; Sarma, D.; Wu, J.; Kanatzidis, M. G. High-Surface-Area Antimony Sulfide Chalcogels. *Chem. Mater.* **2016**, 28 (21), 7744–7749.
- (26) Islam, S. M.; Subrahmanyam, K. S.; Malliakas, C. D.; Kanatzidis, M. G. One-Dimensional Molybdenum Thiochlorides and Their Use in High Surface Area MoS_x Chalcogels. *Chem. Mater.* **2014**, 26 (17), 5151–5160.
- (27) Ahmed, E.; Khanderi, J.; Anjum, D. H.; Rothenberger, A. Selective Adsorption of Volatile Hydrocarbons and Gases in High Surface Area Chalcogels Containing [ES $_3$] $^3-$ Anions (E = As, Sb). *Chem. Mater.* **2014**, 26 (22), 6454–6460.
- (28) Ahmed, E.; Rothenberger, A. KFeSbTe₃: A Quaternary Chalcogenide Aerogel for Preferential Adsorption of Polarizable Hydrocarbons and Gases. *J. Mater. Chem. A* **2015**, 3 (15), 7786–7792.

- (29) Davaasuren, B.; Emwas, A.-H.; Rothenberger, A. MAu₂GeS₄-Chalcogel (M = Co, Ni): Heterogeneous Intra- and Intermolecular Hydroamination Catalysts. *Inorg. Chem.* **2017**, *56* (16), 9609–9616.
- (30) Edhaim, F.; Rothenberger, A. Enhanced Selectivity and Uptake Capacity of CO_2 and Toluene Adsorption in $Co_{0.5}M_{0.33}MoS_4$ (M= Sb or Y) Chalcogels by Impregnated Metal Salts. *ChemistrySelect* **2017**, 2 (32), 10609–10617.
- (31) Edhaim, F.; Rothenberger, A. Preferential Adsorption of Volatile Hydrocarbons on High Surface Area Chalcogels KMBiTe₃(M = Cr, Zn, Fe). *Adv. Powder Technol.* **2018**, 29 (3), 654–663.
- (32) Oh, Y.; Morris, C. D.; Kanatzidis, M. G. Polysulfide Chalcogels with Ion-Exchange Properties and Highly Efficient Mercury Vapor Sorption. J. Am. Chem. Soc. 2012, 134 (35), 14604–14608.
- (33) Riley, B. J.; Chun, J.; Um, W.; Lepry, W. C.; Matyas, J.; Olszta, M. J.; Li, X.; Polychronopoulou, K.; Kanatzidis, M. G. Chalcogen-Based Aerogels As Sorbents for Radionuclide Remediation. *Environ. Sci. Technol.* **2013**, 47 (13), 7540–7547.
- (34) Shafaei-Fallah, M.; He, J.; Rothenberger, A.; Kanatzidis, M. G. Ion-Exchangeable Cobalt Polysulfide Chalcogel. *J. Am. Chem. Soc.* **2011**, 133 (5), 1200–1202.
- (35) Manos, Manolis J.; Kanatzidis, M. G. Layered Metal Sulfides Capture Uranium from Seawater. *J. Am. Chem. Soc.* **2012**, *134* (39), 16441–16446.
- (36) Sarma, D.; Malliakas, C. D.; Subrahmanyam, K. S.; Islam, S. M.; Kanatzidis, M. G. $K_{2x}S_{0+x}S_{0-x}$ (x=0.65-1): A New Metal Sulfide for Rapid and Selective Removal of Cs^+ , Sr^{2+} and UO_2^{2+} Ions. *Chem. Sci.* **2016**, 7 (2), 1121–1132.
- (37) Mertz, J. L.; Fard, Z. H.; Malliakas, C. D.; Manos, M. J.; Kanatzidis, M. G. Selective Removal of Cs^+ , Sr^{2+} , and Ni^{2+} by K_{2x} $Mg_xSn_{3-x}S_6$ (x=0.5-1) (KMS-2) Relevant to Nuclear Waste Remediation. *Chem. Mater.* **2013**, 25 (10), 2116–2127.
- (38) Chupas, P. J.; Qiu, X.; Hanson, J. C.; Lee, P. L.; Grey, C. P.; Billinge, S. J. L. Rapid-Acquisition Pair Distribution Function (RA-PDF) Analysis. *J. Appl. Crystallogr.* **2003**, *36* (6), 1342–1347.
- (39) Hammersley, A. P.; Svensson, S. O.; Hanfland, M.; Fitch, A. N.; Hausermann, D. Two-Dimensional Detector Software: From Real Detector to Idealised Image or Two-Theta Scan. *High Press. Res.* **1996**, *14* (4–6), 235–248.
- (40) Egami, T.; Billinge, S. J. L. Underneath the Bragg Peaks: Structural Analysis of Complex Materials, 2nd ed.; Pergamon materials series; Elsevier: Amsterdam, 2012.
- (41) Juhás, P.; Davis, T.; Farrow, C. L.; Billinge, S. J. L. *PDFgetX3*: A Rapid and Highly Automatable Program for Processing Powder Diffraction Data into Total Scattering Pair Distribution Functions. *J. Appl. Crystallogr.* **2013**, 46 (2), 560–566.
- (42) Farrow, C. L.; Juhas, P.; Liu, J. W.; Bryndin, D.; Božin, E. S.; Bloch, J.; Proffen, T.; Billinge, S. J. L. PDFfit2 and PDFgui: Computer Programs for Studying Nanostructure in Crystals. *J. Phys.: Condens. Matter* **2007**, *19* (33), No. 335219.
- (43) Brinker, C. J.; Scherer, G. W. Sol-Gel Science The Physics and Chemistry of Sol-Gel Processing; Elsevier Inc., 1990.
- (44) Kang, Y. K.; Lee, H.; Ha, T. D. C.; Won, J. K.; Jo, H.; Ok, K. M.; Ahn, S.; Kang, B.; Ahn, K.; Oh, Y.; Kim, M.-G. Thiostannate Coordination Transformation-Induced Self-Crosslinking Chalcogenide Aerogel with Local Coordination Control and Effective Cs+Remediation Functionality. *J. Mater. Chem. A* **2020**, 8 (6), 3468–3480.
- (45) Yuhas, B. D.; Smeigh, A. L.; Douvalis, A. P.; Wasielewski, M. R.; Kanatzidis, M. G. Photocatalytic Hydrogen Evolution from FeMoS-Based Biomimetic Chalcogels. *J. Am. Chem. Soc.* **2012**, *134* (25), 10353–10356.
- (46) Basta, A. H.; Fierro, V.; El-Saied, H.; Celzard, A. 2-Steps KOH Activation of Rice Straw: An Efficient Method for Preparing High-Performance Activated Carbons. *Bioresour. Technol.* **2009**, *100* (17), 3941–3947.
- (47) Pezoti Junior, O.; Cazetta, A. L.; Gomes, R. C.; Barizão, É. O.; Souza, I. P. A. F.; Martins, A. C.; Asefa, T.; Almeida, V. C. Synthesis of ZnCl₂-Activated Carbon from Macadamia Nut Endocarp (Macadamia Integrifolia) by Microwave-Assisted Pyrolysis: Optimi-

- zation Using RSM and Methylene Blue Adsorption. J. Anal. Appl. Pyrolysis 2014, 105, 166–176.
- (48) Arachchige, I. U.; Mohanan, J. L.; Brock, S. L. Sol-Gel Processing of Semiconducting Metal Chalcogenide Xerogels: Influence of Dimensionality on Quantum Confinement Effects in a Nanoparticle Network. *Chem. Mater.* **2005**, *17* (26), 6644–6650.
- (49) Islam, S. M.; Im, J.; Freeman, A. J.; Kanatzidis, M. G. Ba₂HgS₅—A Molecular Trisulfide Salt with Dumbbell-like (HgS₂)²-Ions. *Inorg. Chem.* **2014**, 53 (9), 4698–4704.
- (50) Islam, S. M.; Sangwan, V. K.; Li, Y.; Kang, J.; Zhang, X.; He, Y.; Zhao, J.; Murthy, A.; Ma, S.; Dravid, V. P.; Hersam, M. C.; Kanatzidis, M. G. Abrupt Thermal Shock of (NH₄)₂Mo₃S₁₃ Leads to Ultrafast Synthesis of Porous Ensembles of MoS₂ Nanocrystals for High Gain Photodetectors. *ACS Appl. Mater. Interfaces* **2018**, *10* (44), 38193–38200.
- (51) Hassanzadeh Fard, Z.; Islam, S. M.; Kanatzidis, M. G. Porous Amorphous Chalcogenides as Selective Adsorbents for Heavy Metals. *Chem. Mater.* **2015**, 27 (18), 6189–6192.
- (52) Müller, A.; Sarkar, S.; Bhattacharyya, R. G.; Pohl, S.; Dartmann, M. Directed Synthesis of $[Mo_3S_{13}]^{2-}$, an Isolated Cluster Containing Sulfur Atoms in Three Different States of Bonding. *Angew. Chem., Int. Ed. Engl.* **1978**, *17* (7), 535–535.
- (53) Mueller, A.; Nolte, W. O.; Krebs, B. $(NH_4)_2[(S_2)_2Mo(S_2)_2Mo(S_2)_2]$. 2H₂O, a Novel Sulfur-Rich Coordination Compound with Two Nonequivalent Complex Anions Having the Same Point Group but Different Structures: Crystal and Molecular Structures. *Inorg. Chem.* **1980**, 19 (9), 2835–2836.
- (54) Islam, S. M.; Cain, J. D.; Shi, F.; He, Y.; Peng, L.; Banerjee, A.; Subrahmanyam, K. S.; Li, Y.; Ma, S.; Dravid, V. P.; Grayson, M.; Kanatzidis, M. G. Conversion of Single Crystal (NH₄)₂Mo₃S₁₃·H₂O to Isomorphic Pseudocrystals of MoS₂ Nanoparticles. *Chem. Mater.* **2018**, *30* (11), 3847–3853.
- (55) Sarma, D.; Islam, S. M.; Subrahmanyam, K. S.; Kanatzidis, M. G. Efficient and Selective Heavy Metal Sequestration from Water by Using Layered Sulfide $K_{2x}Sn_{4-x}S_{8-x}$ (x=0.65-1;KTS-3). *J. Mater. Chem. A* **2016**, *4* (42), 16597–16605.
- (56) Islam, S. M.; Vanishri, S.; Li, H.; Stoumpos, C. C.; Peters, John A.; Sebastian, M.; Liu, Z.; Wang, S.; Haynes, A. S.; Im, J.; Freeman, A. J.; Wessels, B.; Kanatzidis, M. G. Cs₂Hg₃S₄: A Low-Dimensional Direct Bandgap Semiconductor. *Chem. Mater.* **2015**, *27* (1), 370–378.
- (57) Islam, S. M.; Malliakas, C. D.; Sarma, D.; Maloney, D. C.; Stoumpos, C. C.; Kontsevoi, O. Y.; Freeman, A. J.; Kanatzidis, M. G. Direct Gap Semiconductors Pb₂BiS₂I₃, Sn₂BiS₂I₃, and Sn₂BiSI₅. *Chem. Mater.* **2016**, 28 (20), 7332–7343.
- (58) Seo, B.; Jung, G. Y.; Lee, S. J.; Baek, D. S.; Sa, Y. J.; Ban, H. W.; Son, J. S.; Park, K.; Kwak, S. K.; Joo, S. H. Monomeric MoS₄²⁻-Derived Polymeric Chains with Active Molecular Units for Efficient Hydrogen Evolution Reaction. *ACS Catal.* **2020**, *10* (1), 652–662.
- (59) Wang, C.; Chen, S.; Xie, H.; Wei, S.; Wu, C.; Song, L. Atomic Sn⁴⁺ Decorated into Vanadium Carbide MXene Interlayers for Superior Lithium Storage. *Adv. Energy Mater.* **2019**, 9 (4), No. 1802977.
- (60) Jumas, J.-C.; Philippot, E.; Vermot-Gaud-Daniel, F.; Ribes, M.; Maurin, M. Etude de la tétracoordination de l'etain dans deux orthothiostannates: Na_4SnS_4 et Ba_2SnS_4 (α). J. Solid State Chem. 1975, 14 (4), 319–327.
- (61) Hazen, R. M.; Finger, L. W. The Crystal Structures and Compressibilities of Layer Minerals at High Pressure; I, SnS < 2), Berndtite. *Am. Mineral.* **1978**, 63 (3–4), 289–292.
- (62) Jumas, J.-C.; Philippot, E.; Maurin, M. Etude structurale de Na₄Sn₃S₈. Evolution de la coordination de l'etain dans le système Na₂S-SnS₂. *J. Solid State Chem.* **1975**, *14* (2), 152–159.
- (63) Newville, M. Larch: An Analysis Package for XAFS and Related Spectroscopies. J. Phys. Conf. Ser. 2013, 430 (1), No. 012007.
- (64) Wignacourt, J. P.; Drache, M.; Swinnea, J. S.; Steinfink, H.; Lorriaux-Rubbens, A.; Wallart, F. Crystal Structure and Raman Scattering Investigation of Anhydrous $(NH_4)_2[MO_2(S_2)_6]$. Cand. J. Appl. Spec. 1992, 37, 49–54.

- (65) Behrens, E. A.; Sylvester, P.; Clearfield, A. Assessment of a Sodium Nonatitanate and Pharmacosiderite-Type Ion Exchangers for Strontium and Cesium Removal from DOE Waste Simulants. *Environ. Sci. Technol.* **1998**, 32 (1), 101–107.
- (66) Riley, B. J.; Chong, S. Environmental Remediation with Functional Aerogels and Xerogels. *Glob. Chall.* **2020**, 4 (10), No. 2000013.
- (67) Zeng, X.; Zeng, M.; Zhang, T.; Cai, P.-W.; Feng, M.-L.; Huang, X.-Y. Efficient Uptake of Uranium(VI) by a Layered Manganese Thiophosphite Intercalated with NH4+. *Chem. Eng. J.* **2022**, 429, No. 132474.
- (68) Manos, M. J.; Kanatzidis, M. G. Metal Sulfide Ion Exchangers: Superior Sorbents for the Capture of Toxic and Nuclear Waste-Related Metal Ions. *Chem. Sci.* **2016**, *7* (8), 4804–4824.